

Supplementary information

All-perovskite tandem solar cells with improved grain surface passivation

In the format provided by the
authors and unedited

Supplementary Information for:

All-perovskite tandem solar cells with improved grain surface passivation

Renxing Lin,^{1†} Jian Xu,^{2†} Mingyang Wei,^{2†} Yurui Wang,^{1†} Zhengyuan Qin,^{3†} Zhou Liu,¹ Jinlong Wu,¹ Ke Xiao,^{1,4} Bin Chen,² So Min Park,² Gang Chen,⁵ Harindi R. Atapattu,⁶ Kenneth R. Graham,⁶ Jun Xu,⁴ Jia Zhu,¹ Ludong Li,¹ Chunfeng Zhang,³ Edward H. Sargent^{2*} & Hairen Tan^{1,7*}

¹*National Laboratory of Solid State Microstructures, Collaborative Innovation Center of Advanced Microstructures, Jiangsu Key Laboratory of Artificial Functional Materials, College of Engineering and Applied Sciences, Nanjing University, Nanjing 210023, China.*

²*Department of Electrical and Computer Engineering, University of Toronto, 10 King's College Road, Toronto, Ontario, M5S 3G4, Canada.*

³*School of Physics, Nanjing University, Nanjing 210093, China.*

⁴*School of Electronic Science and Engineering, Nanjing University, Nanjing 210023, China.*

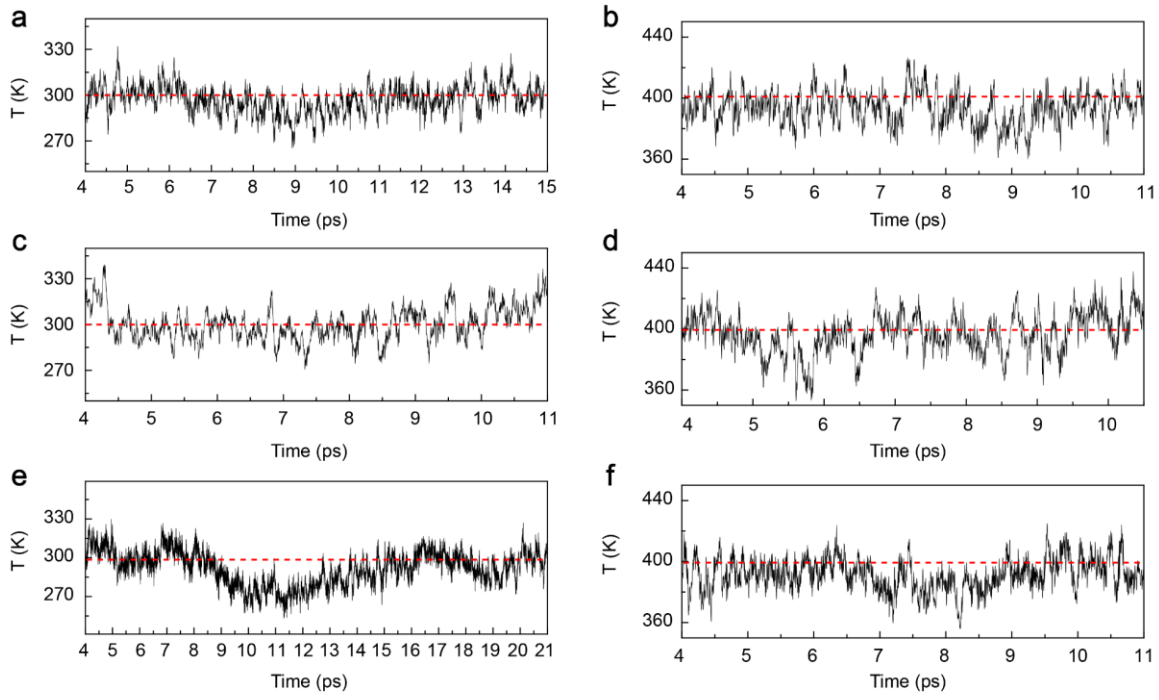
⁵*School of Physical Science and Technology, ShanghaiTech University, Shanghai, 201210 China*

⁶*Department of Chemistry, University of Kentucky, Lexington, Kentucky 40506, United States*

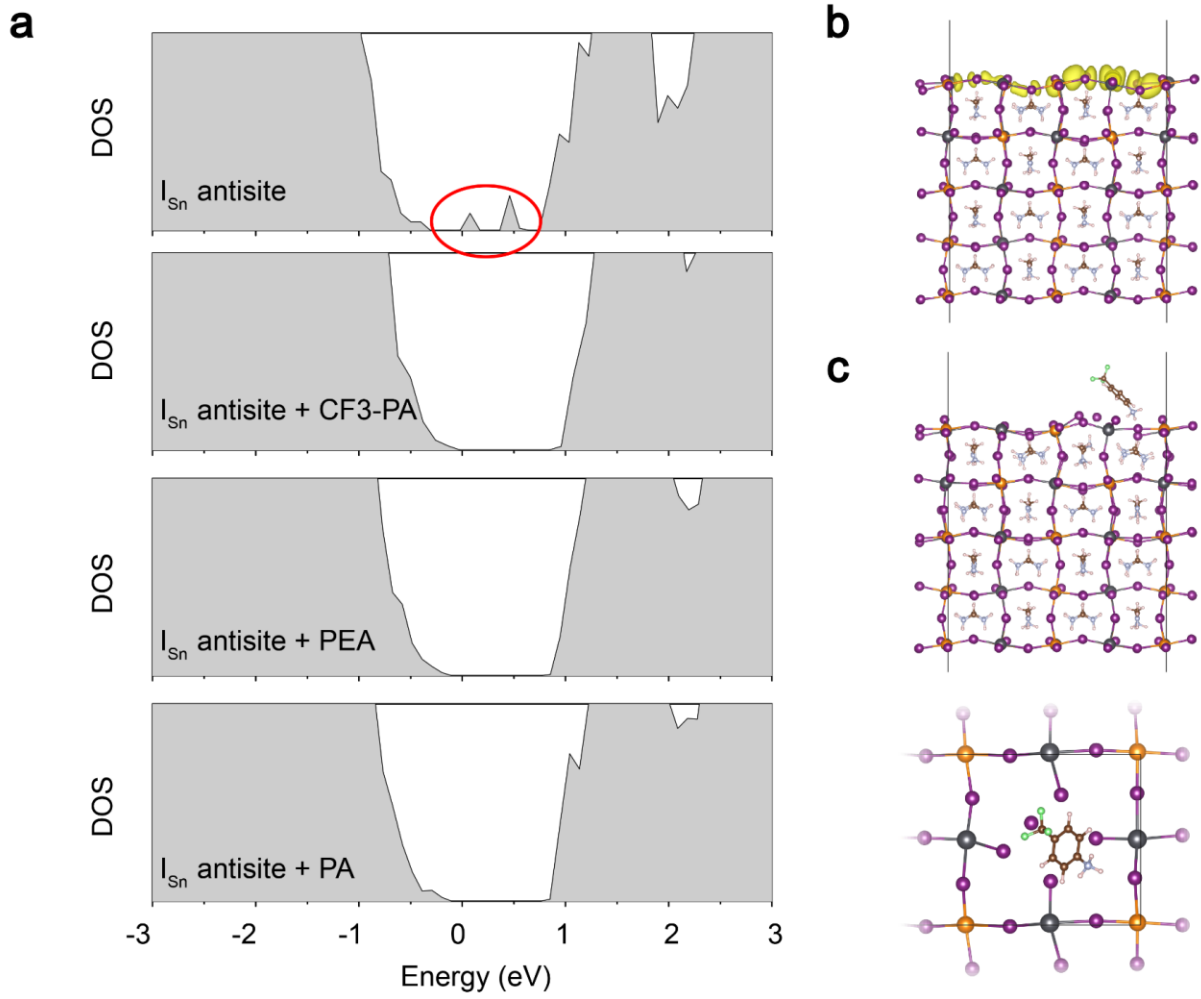
⁷*Frontiers Science Center for Critical Earth Material Cycling, Nanjing University, Nanjing 210023, China*

† These authors contributed equally to this work.

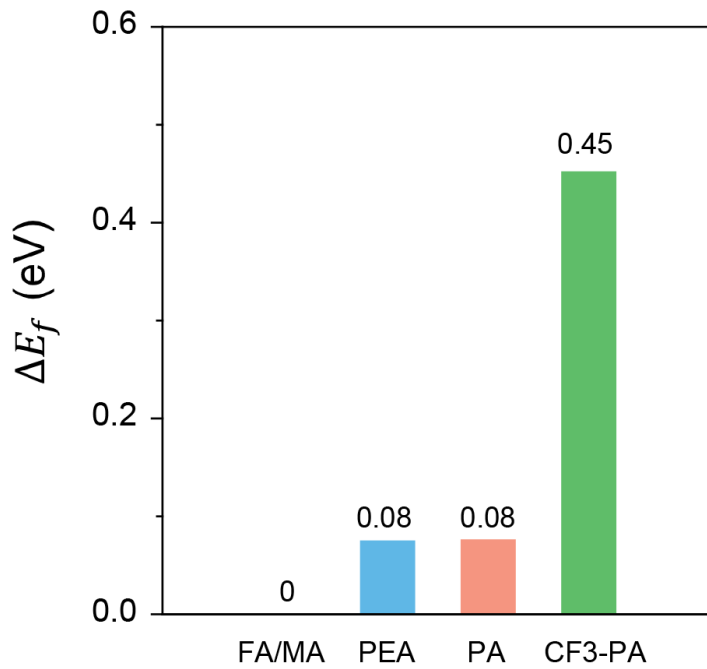
*Corresponding authors. E-mails: hairentan@nju.edu.cn (H.T.); ted.sargent@utoronto.ca (E.H.S)



Supplementary Figure 1 | Temperature fluctuation of ab initio molecular dynamics simulations. The temperature (T) as function of time in molecular dynamic simulations at a targeted T of (a, c, e) 300K and (b, d, f) 400K for (a, b) CF3-PA, (c, d) PA, (e, f) PEA adsorbed perovskite surface. The simulations were run for 10~20 ps.



Supplementary Figure 2 | Effect of cationic passivators on the surface deep-level defect. **a**, Density of states (DOS) of the surface I_{Sn} antisite defect with or without cationic passivator (CF3-PA, PA or PEA) treatment. **b**, Partial charge density of the in-gap states in (a) highlighted with red circle. **c**, Adsorption configuration of the CF3-PA on the perovskite surface with I_{Sn} antisite defect. Pb, grey; Sn, orange; F, green; N, silver; I, purple; C, brown; H, light pink.

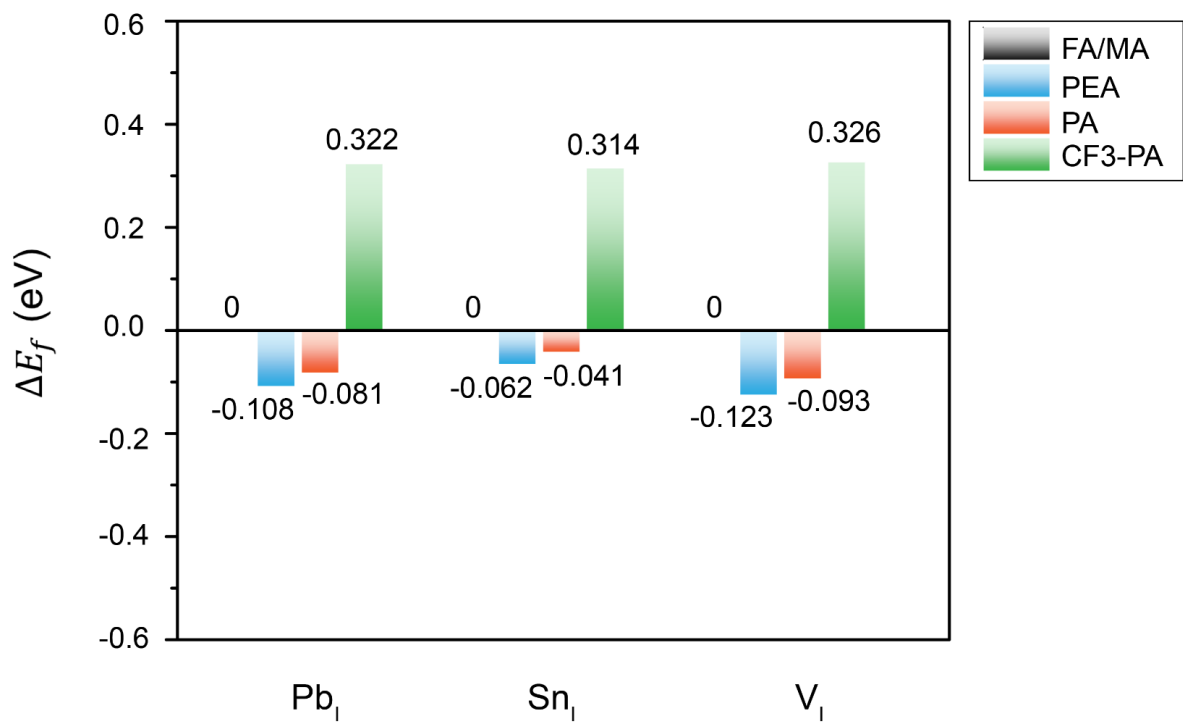


Supplementary Figure 3 | Relative formation energies (ΔE_f) of the V_{Sn} in CF3-PA, PA and PEA fully occupied perovskite surface, with respect to the original FA/MA occupied case.

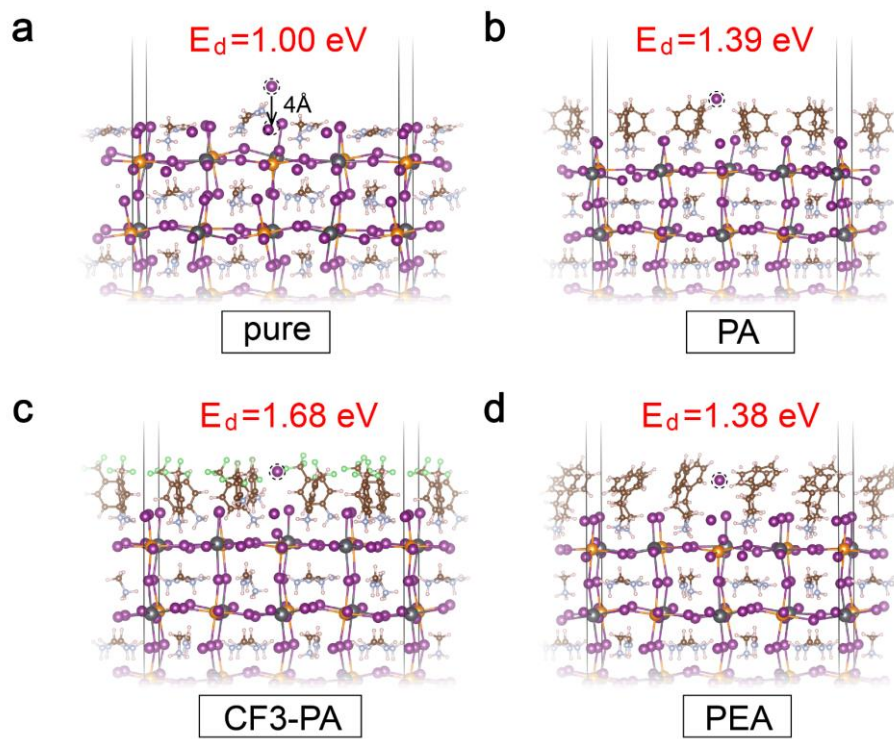
Supplementary Note 1:

Ammonium cation passivation on the formation of donor-like defects

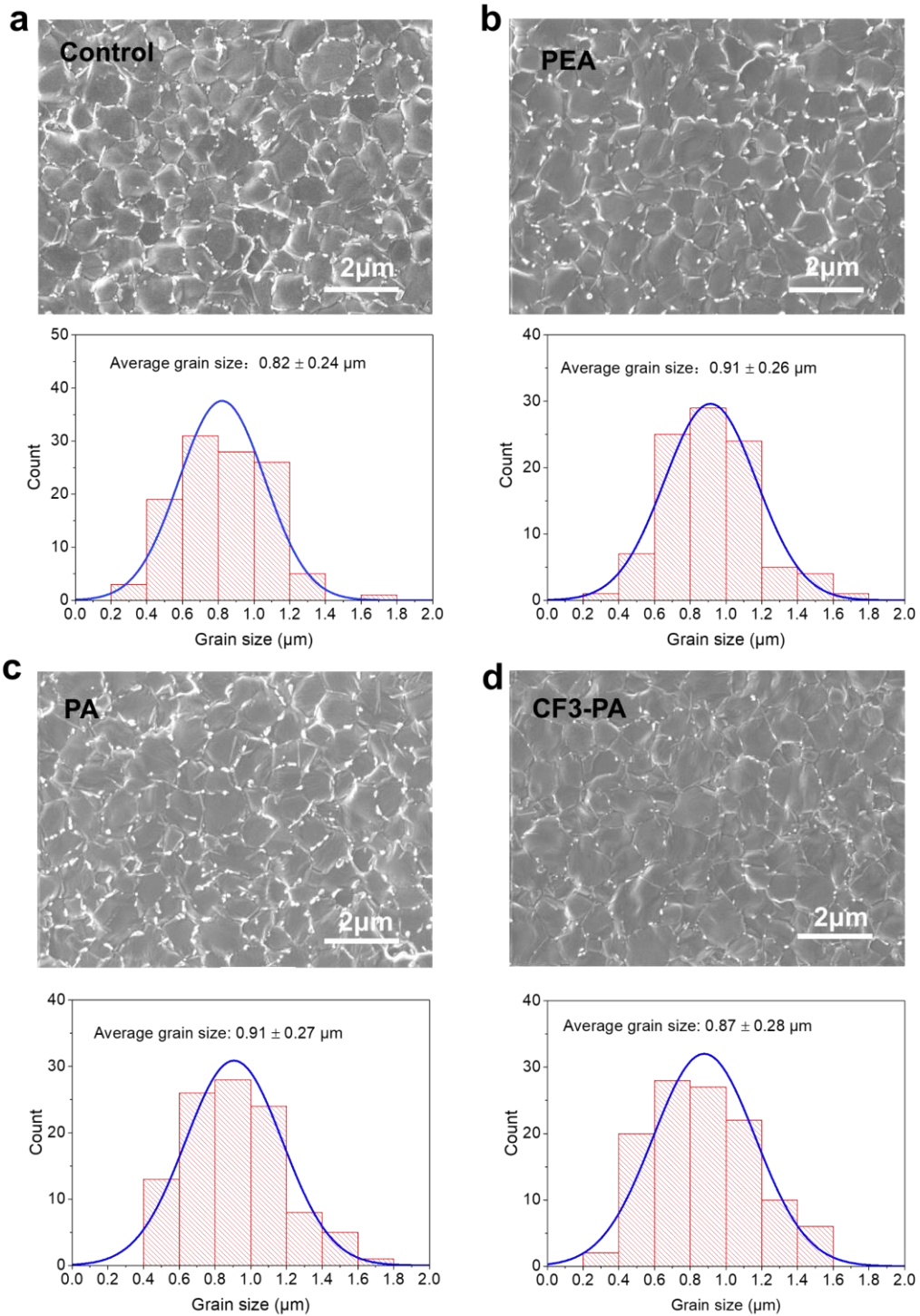
We further investigated the effect of PEA, PA, and CF3-PA passivators on the formation of donor-like defects, *e.g.* iodine vacancies (V_I), Sn substituted at the iodine site (Sn_I), and Pb substituted at the iodine site (Pb_I). When we posit that all FA/MA vacancies on the A-I terminated perovskite surface are occupied by the passivation agents (**Supplementary Fig. 4**), we find that CF3-PA has higher defect formation energies than PA and PEA, which indicates that these donor-like defects become less favorable to form after CF3-PA treatment. We calculated the relative desorption energies (E_d) of iodide ions from the perovskite surface passivated with the three passivators (**Supplementary Fig. 5**). The increased desorption energy indicates that CF3-PA suppresses the iodine detachment from perovskite surface (which otherwise create iodine vacancies), in accordance with the dynamic simulation shown in **Fig. 1c**.



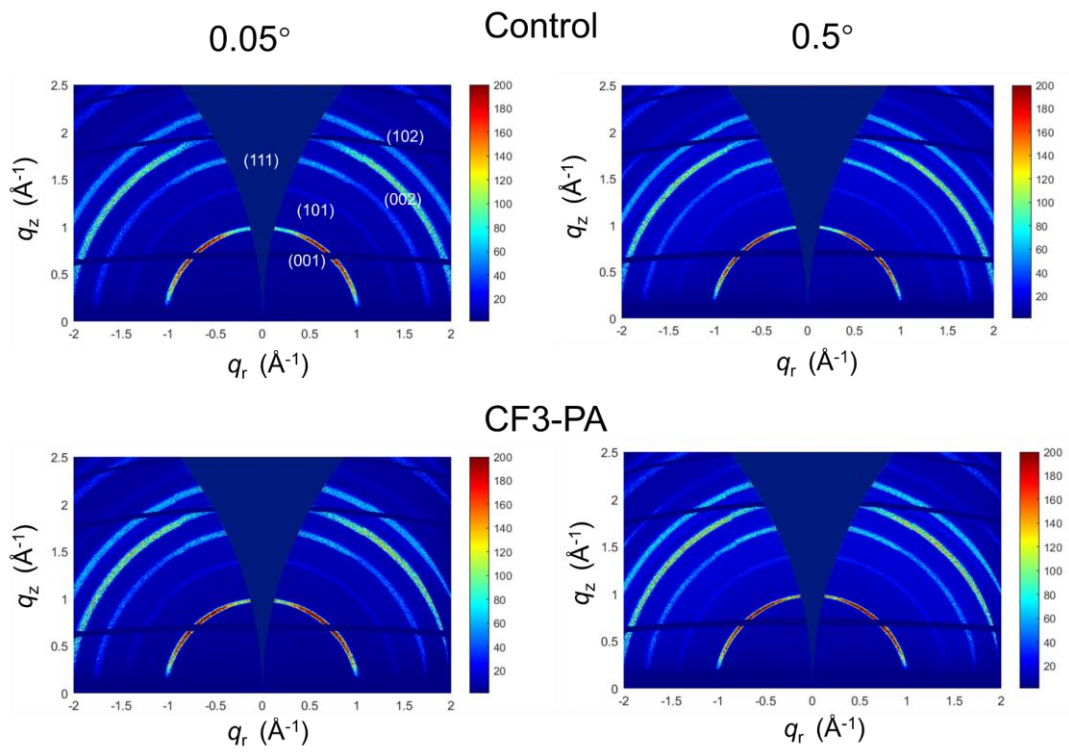
Supplementary Fig. 4 | Relative formation energies (ΔE_f) of the donor-like defects (V_I, Sn_I and Pb_I) in CF3-PA, PA and PEA fully occupied perovskite surface, with respect to the original FA/MA occupied case.



Supplementary Figure 5 | Relative desorption energies (E_d) of I^- ions from the surfaces passivated with different cationic ions. DFT-relaxed configurations of iodine migration on the **a**, FA/MA, **b**, PA, **c**, CF3-PA and **d**, PEA fully occupied perovskite surface. The migrating I^- ions denoted by dashed circles are fixed at a distance of $\sim 4 \text{ \AA}$ along the z-direction away from the perovskite surface.



Supplementary Figure 6 | SEM image and grain size distribution of 1200-nm-thick **(a)** control, **(b)** PEA, **(c)** PA and **(d)** CF3-PA mixed Pb-Sn perovskite films. The samples were processed at the same runs.

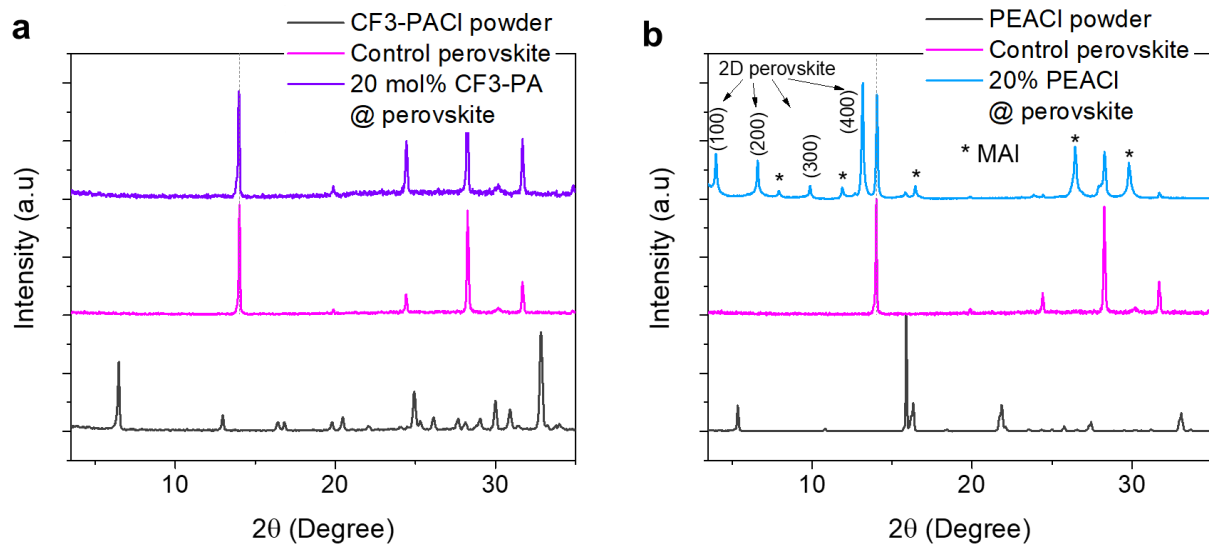


Supplementary Figure 7 | GIWAXS patterns of control (upper) and CF3-PA (lower) Pb-Sn perovskite films measured at incident angles of 0.05° and 0.5° .

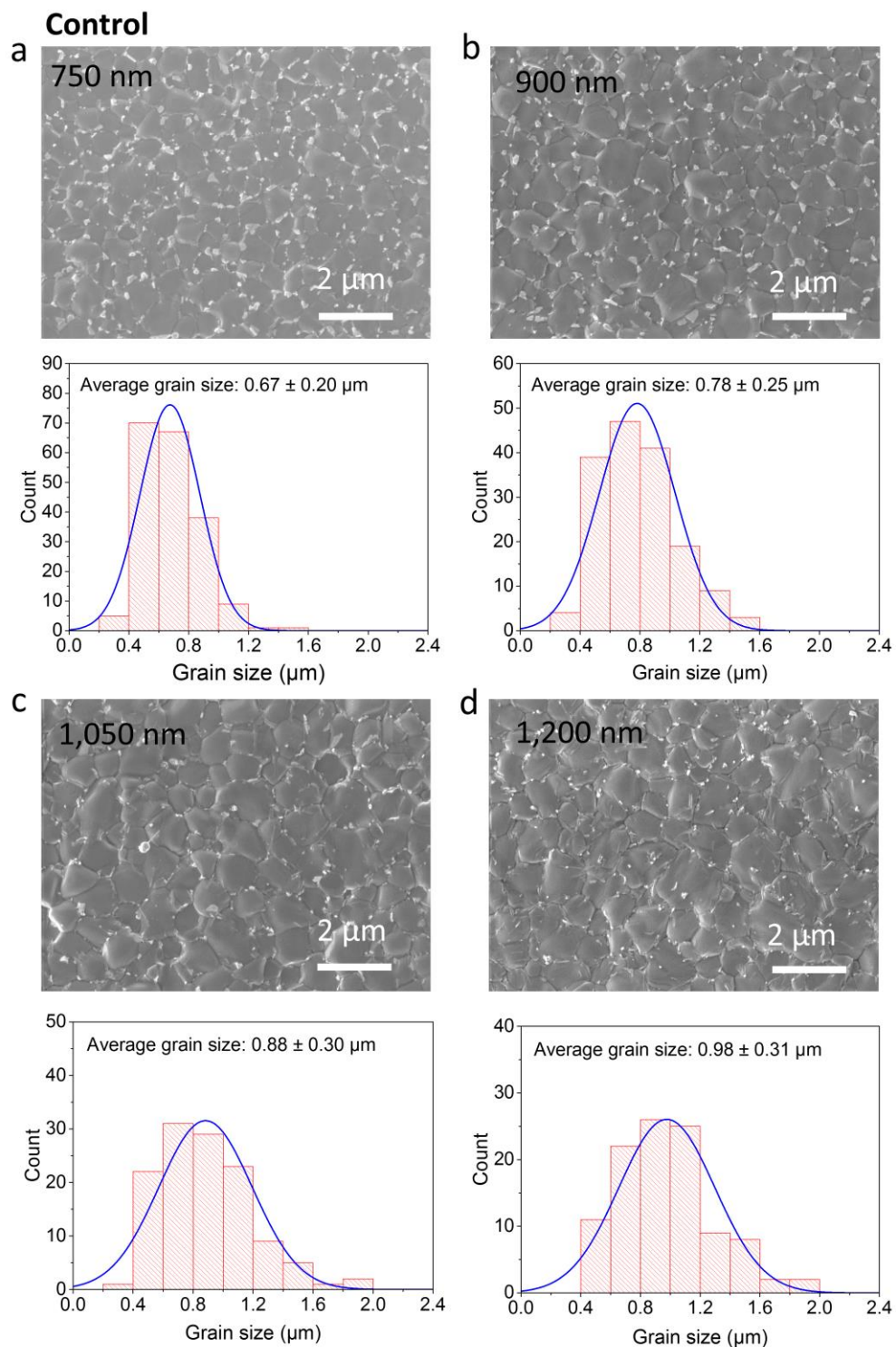
Supplementary Note 2:

Extended structural characterization on Pb-Sn perovskite thin films

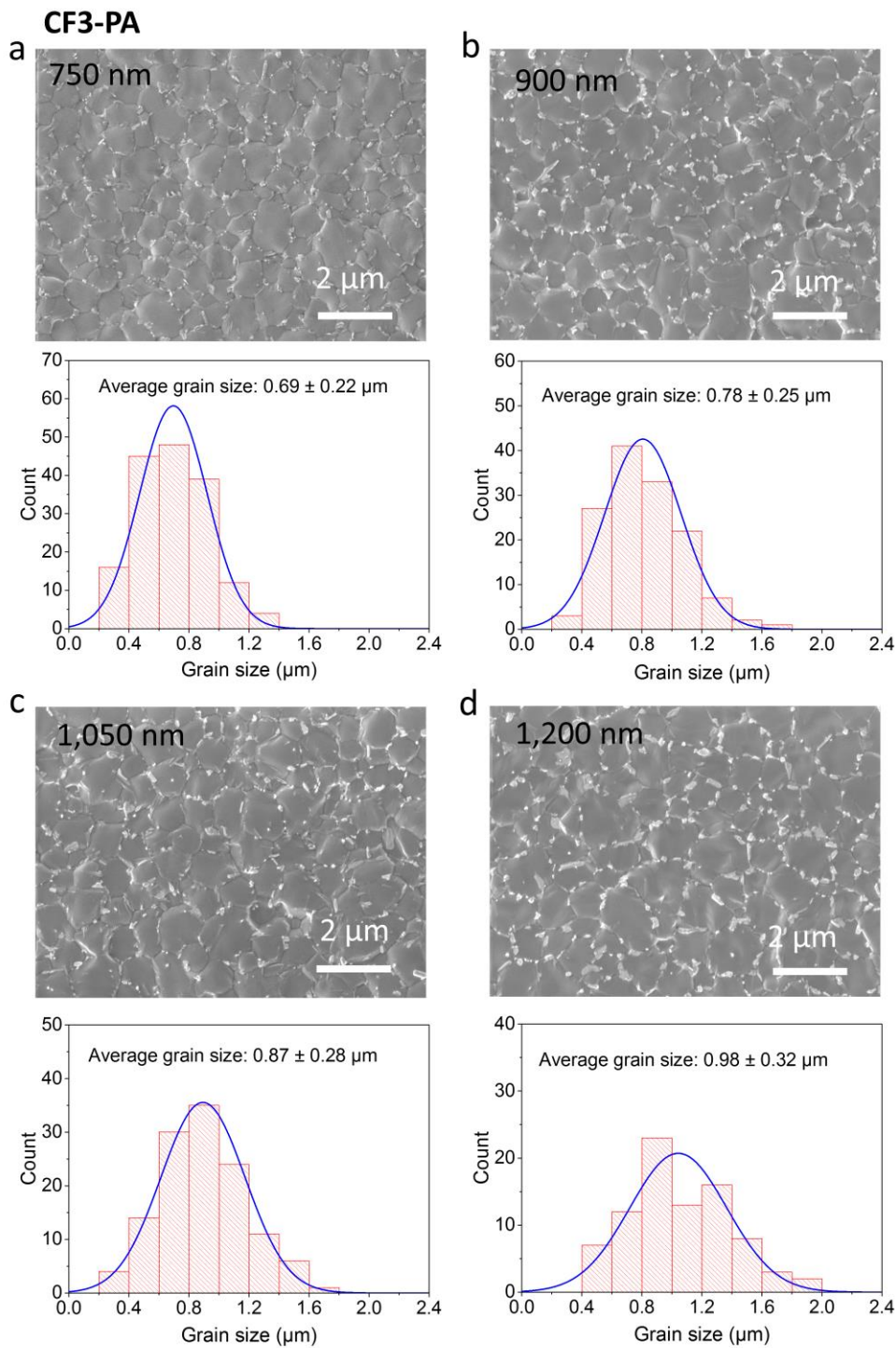
Grain surface passivation can be realized through the templated growth of 2D layered perovskites atop 3D perovskites or through the direct anchoring of ammonium cations on the perovskite grain surfaces¹⁻³. The formation of 2D/3D heterostructures would otherwise hinder charge transport particularly in thick-absorber devices^{4,5}. We found 2D layered perovskite phase remained absent within the perovskite film, when 20 mol% of CF3-PA was added in the precursor solution (**Supplementary Fig. 8**). By contrast, substantial 2D perovskite phase was formed within the film when 20 mol% of PEA was added. We further carried out SEM and XRD studies of control and CF3-PA mixed Pb-Sn perovskite films with different thicknesses, revealing no noticeable difference on the surface morphology, grain size, crystal structure and crystallinity between control and CF3-PA films at the same thickness (**Supplementary Fig. 9-11**).



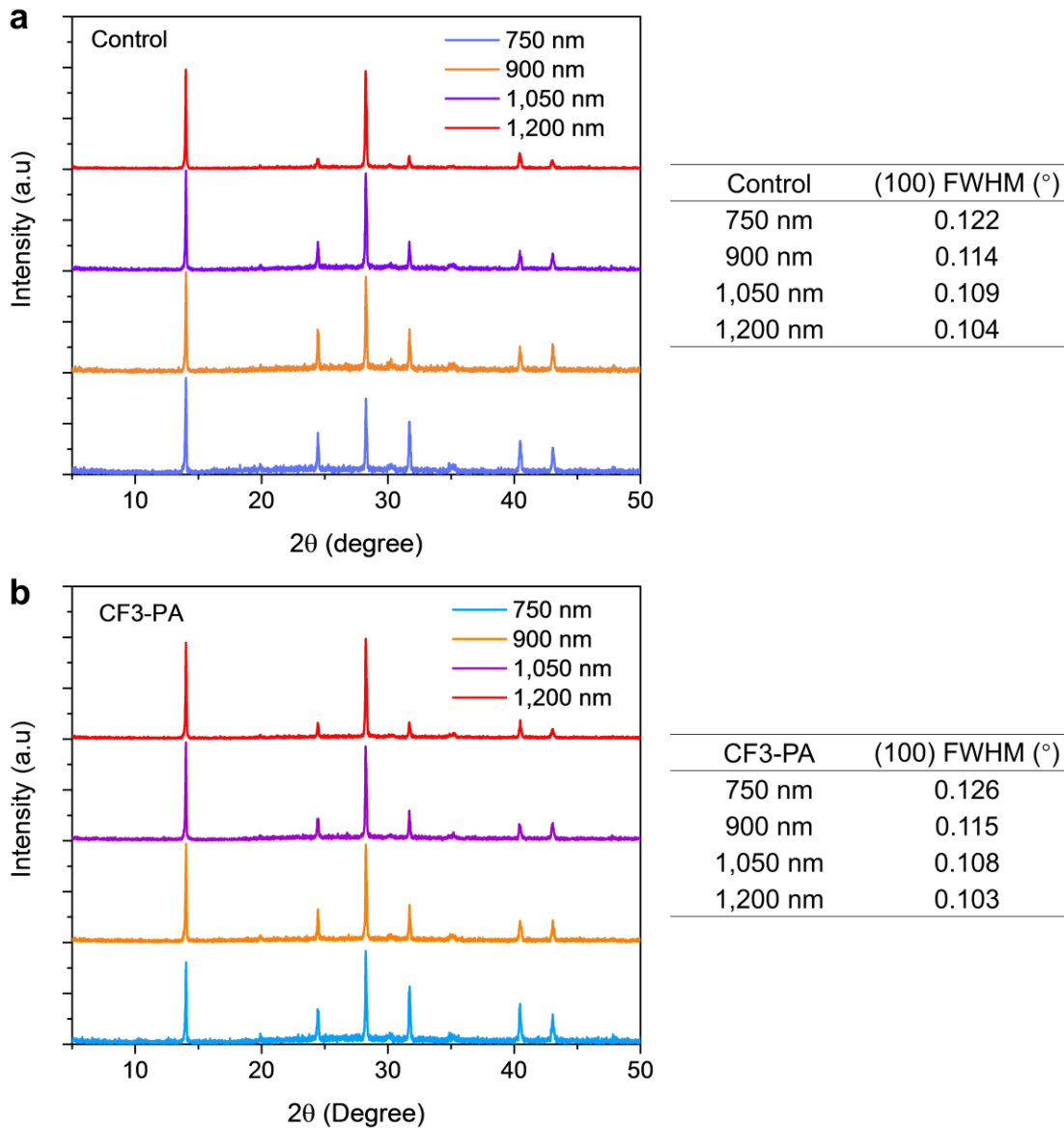
Supplementary Figure 8 | XRD patterns of Pb-Sn perovskite films with a large amount (20 mol%) of passivating agents added into the precursor solution. **a**, XRD patterns of the CF3-PACl powders, control and CF3-PA (20 mol%) perovskite films. **b**, XRD patterns of the PEACl powders, control and PEA (20 mol%) perovskite films.



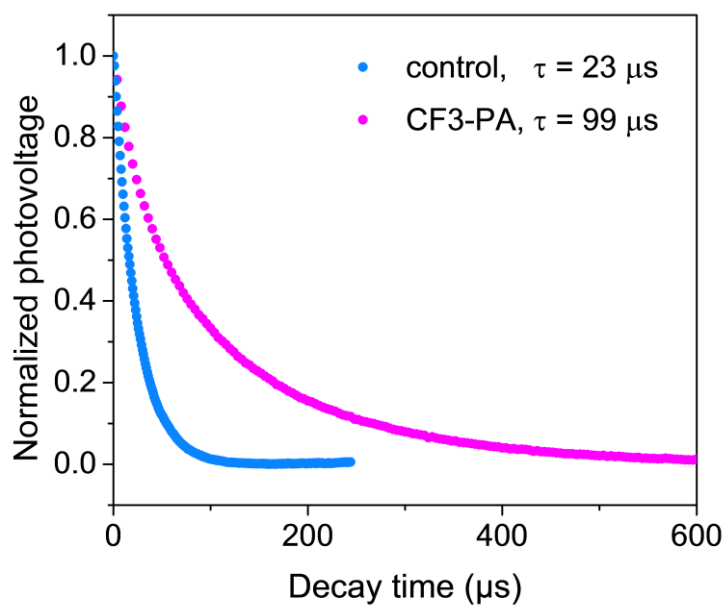
Supplementary Figure 9 | SEM image and grain size distribution of control mixed Pb-Sn perovskite films with thicknesses of 750, 900, 1,050 and 1,200 nm.



Supplementary Figure 10 | SEM image and grain size distribution of CF3-PA mixed Pb-Sn perovskite films with thicknesses of 750, 900, 1,050 and 1,200 nm. Note that samples shown in Supplementary Figs. 9 and 10 were processed at the same runs.



Supplementary Figure 11 | XRD patterns and corresponding full width at half maximum (FWHM) of (100) diffraction peak of (a) control and (b) CF3-PA mixed Pb-Sn perovskite films with different thicknesses.



Supplementary Figure 12 | Transient photovoltage measurements of control and CF3-PA mixed Pb-Sn perovskite solar cells.

Supplementary Note 3:

1. Derivation of charge carrier mobility (μ_{dc}) from OPTP measurements

Briefly, we analyzed the complex photoconductivity $\Delta\tilde{\sigma}(\omega, \tau)$ using the Drude-Smith model,

$$\Delta\tilde{\sigma}(\omega, \tau) = \frac{\varepsilon_0\omega_p^2\tau}{1-i\omega\tau} \left[1 + \frac{c_1}{1-i\omega\tau} \right], \quad (S1)$$

where the first item is the Drude conductivity, while the second Smith term modifies the Drude model by accounting for the backscattering of carriers due to the influence of disorder in the films.

The model consists of three free parameters: ω_p , τ , and c_1 which can be obtained by fitting the experimental data (see **Supplementary Figure 13**). The free charge density can be derived from the Drude plasma frequency ω_p as $n = \varepsilon_0\omega_p^2m^*/e^2$ with effective mass $m^* = 0.2m$, ε_0 is the vacuum permittivity and e is the electron charge. The average time interval τ between collision events described the carrier scattering rate which is related to the carrier mobility via the expression $\mu = e\tau/m^*$. The parameter c_1 describes the strength of backscattering, ranging between -1 (complete backscattering) and 0 (no backscattering). Hence the effective carrier mobility becomes $\mu_{dc} = e(1 + c_1)\tau/m^*$, according the Drude-Smith model.

2. Calculating the mobility of limiting carrier ($\mu_{e,h}$) and diffusion length (L_d)

We measured the OPTP transients pumped at 3.1 eV and 1.55 eV, respectively. For the perovskite films covered with a C₆₀ layer on top the pump pulses were excited from the C₆₀ side. Since the surface carriers are extracted from the C₆₀ layer, the decay of photo-induced THz signal can be observed within a 2-ns time window. We assume that the mobility does not change with time delay, then the concentration of photo-induced carriers is proportional to the photo-induced

change of THz signals. The measured OPTP kinetics (see **Supplementary Figure 14**) can be modelled with diffusion and surface recombination model, the detailed description of which can be found in previously published literature [Hempel et al., *Sci Rep* **8**, 14476 (2018)].

$$\frac{d}{dt} \Delta n = g - \frac{\Delta n}{\tau_B} + D_{am} \frac{d^2}{dx^2} \Delta n \quad (\text{S2})$$

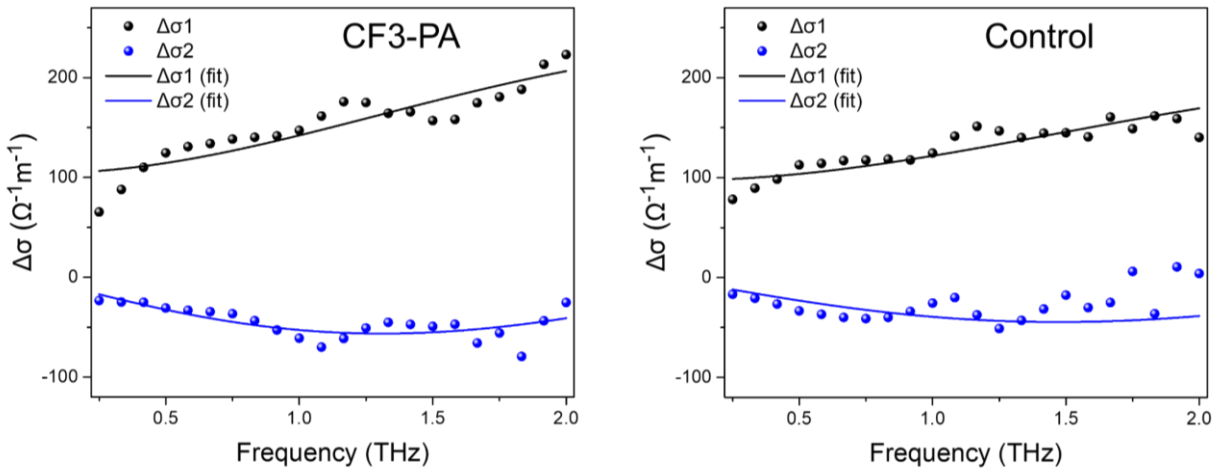
$$\Delta n(x, 0) = N_0 \exp(-\alpha x) \quad (\text{S3})$$

$$D_{am} \frac{d}{dx} \Delta n|_{x=0} = -S \Delta n \quad (\text{S4})$$

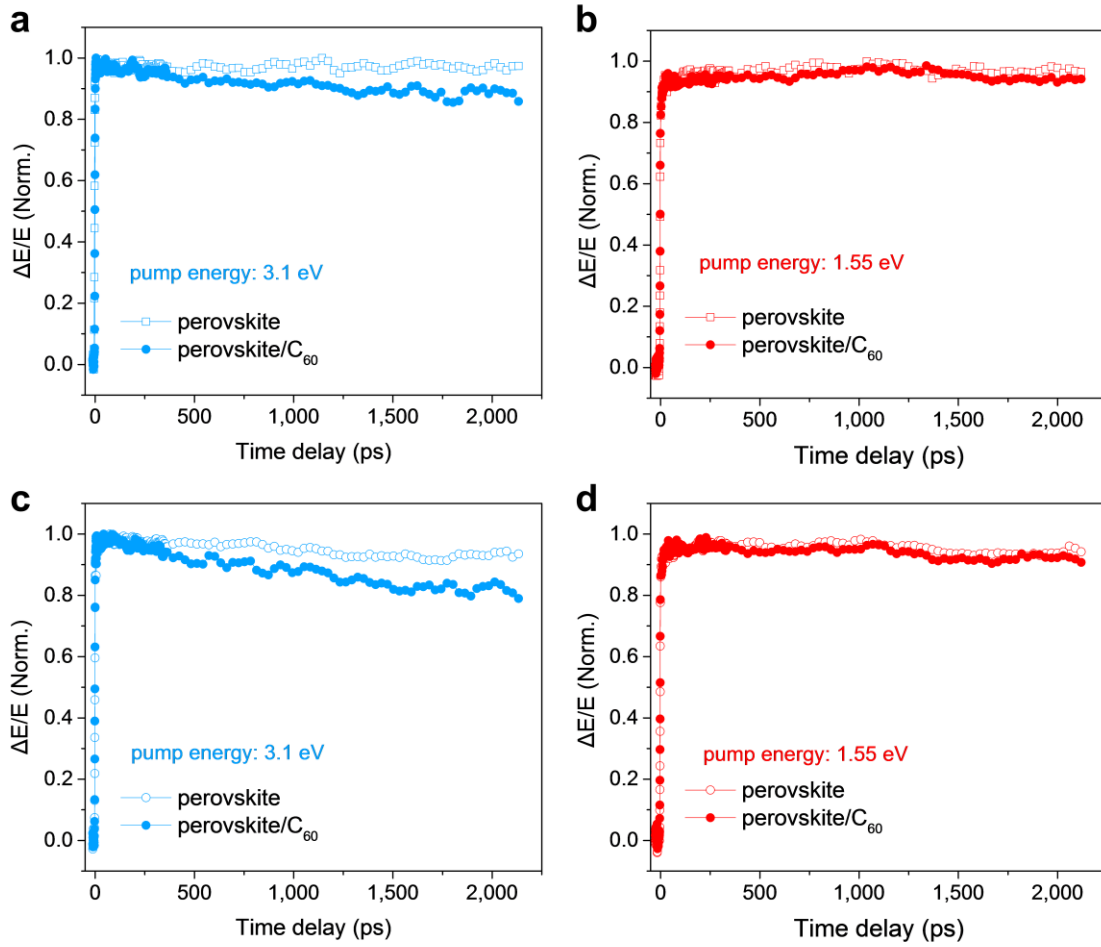
$$D_{am} = 2 \frac{\mu_e \mu_h}{\mu_e + \mu_h} \frac{k_B T}{e} \quad (\text{S5})$$

Here, Δn is the concentration of the photo-induced carriers, g is the generation rate of the photo-induced carriers, D_{am} is the ambipolar diffusion coefficient and τ_B is the bulk carrier lifetime. τ_B is on the order of tens of ns, which is obtained from ns-resolved OPTP transient. The initial condition for equation S2 is assumed to obey Lambert-Beer law, in the form of equation S3. The characteristic absorption depths ($1/\alpha$) of 585 nm and 85 nm are calculated for the 1.5 eV and 3.1 eV pumped photons, respectively, as obtained from the UV-VIS spectrum. The boundary condition can be described by the equation S4. For the front surface covered with a C₆₀ layer, surface recombination (S) will dominate. Here, surface recombination (S) includes the carrier extraction of the C₆₀ layer and non-radiative recombination assisted by traps at the interface. Since the film thickness is much larger than the characteristic absorption depths, we assume the film as a semi-infinite semiconductor slab. The model consists of two free parameters: D_{am} and S , which can be obtained by fitting the OPTP transients. Since the photo-induced carrier concentration is much larger than the intrinsic carrier concentration of the unexcited film, the ambipolar diffusion coefficient can be connected to the individual mobilities of electrons and holes by equation S5

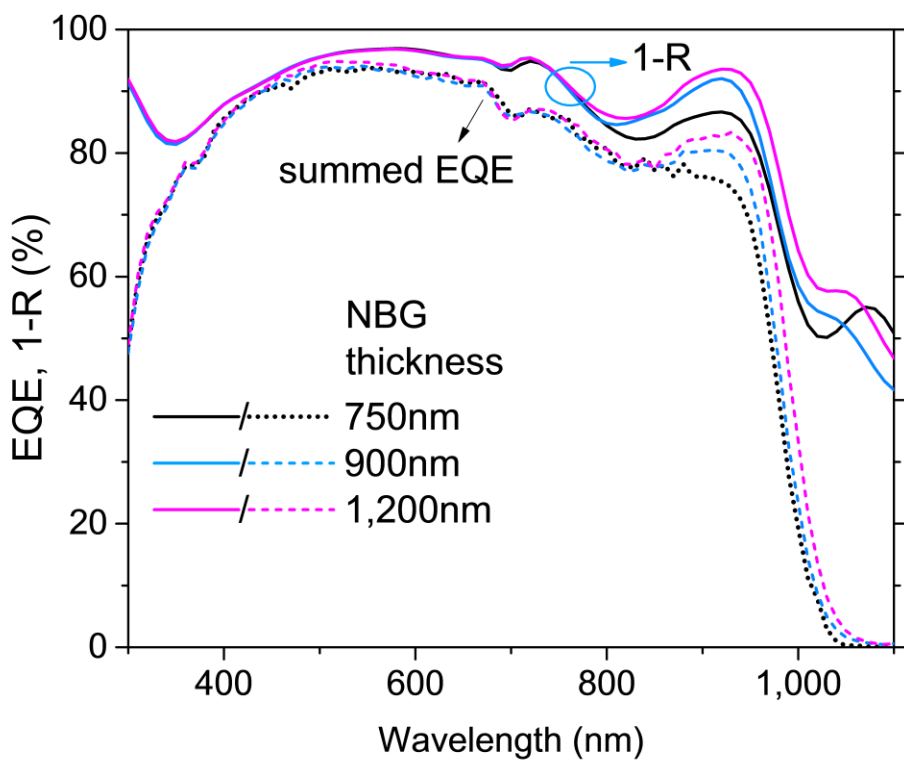
with Einstein relationship, where k_b is the Boltzmann's constant, T is the temperature in K (295 K in our case), and e is the elementary charge. Combined with the DC mobility ($\mu_{dc} = \mu_e + \mu_h$) obtained from the complex photoconductivity as mentioned above, we can extract individual mobilities. Although we cannot distinguish the mobilities of electron or hole, we can obtain the minority carrier mobility (mobility of limiting carrier type). The minority carrier diffusion length is then calculated according to the equation of $L_d = \sqrt{\mu_{e,h} k_B T \tau / e}$, where the carrier lifetime τ is obtained from the time-resolved PL measurements.



Supplementary Figure 13 | THz spectra of CF3-PA and control Pb-Sn perovskite films deposited on quartz substrates. Frequency-dependent complex THz conductivity ($\Delta\sigma = \Delta\sigma_1 + i\Delta\sigma_2$) at different time delays for the control and CF3-PA samples. The solid lines are curves fitting to the Drude-Smith model. The summed DC mobilities (μ_{dc}) of CF3-PA and control samples are calculated to be 82 ± 2 and $79 \pm 1 \text{ cm}^2 \text{ V}^{-1} \text{ s}^{-1}$ (average value of 4 samples for each type), respectively.

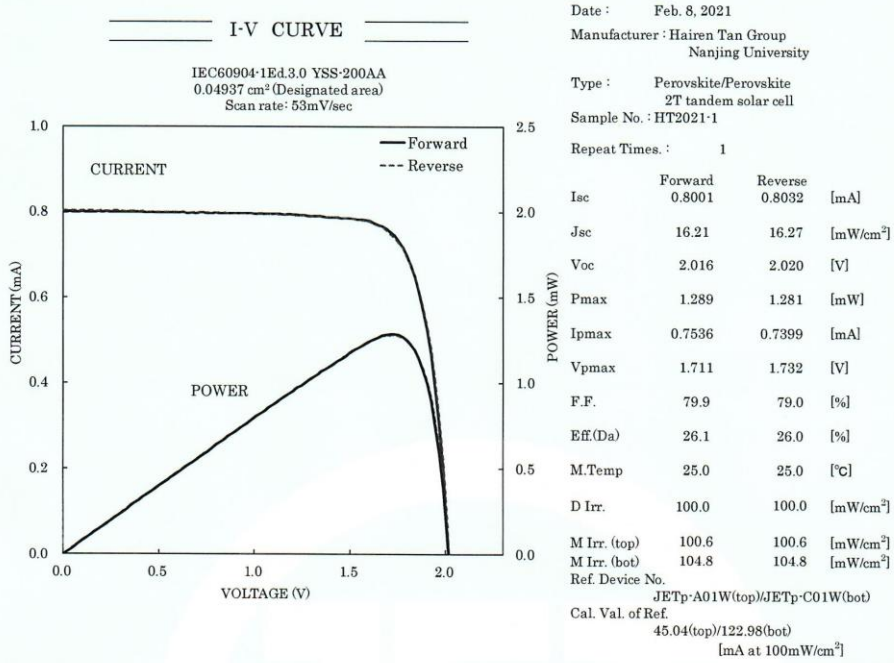


Supplementary Figure 14 | THz spectra of CF3-PA and control Pb-Sn perovskite films with and without C_60 on top. **a,b**, femtosecond OOPTP transients for control samples. **c,d**, femtosecond OOPTP transients for CF3-PA perovskite films. The transients are measured after excitation with photon wavelengths of 400 nm (photon energy of 3.1 eV) and 800 nm (photon energy of 1.55 eV).

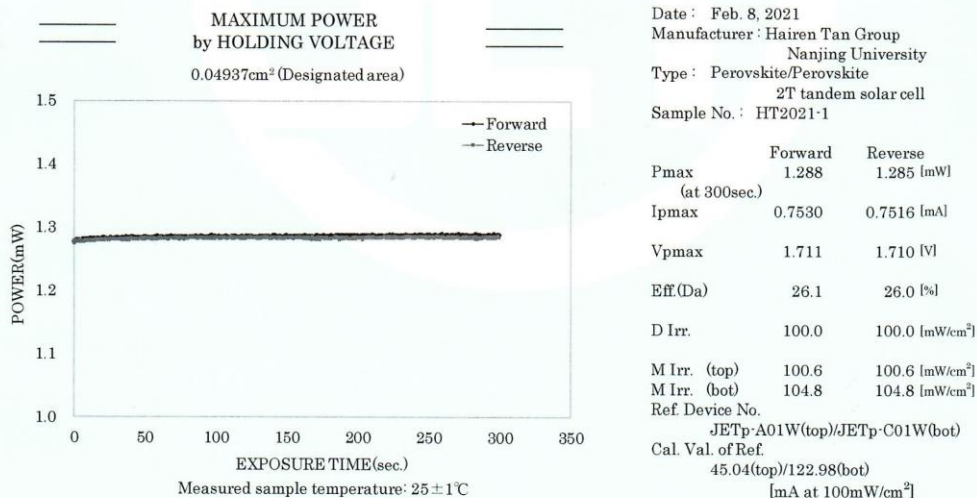


Supplementary Figure 15| Summed EQE and total absorptance ($1-R$) curves of tandem cells with back subcell thickness of 750, 900, and 1,200 nm (referred to devices shown in Fig. 4c).

測定成績書番号(Reference No. 20TR-PV0029)

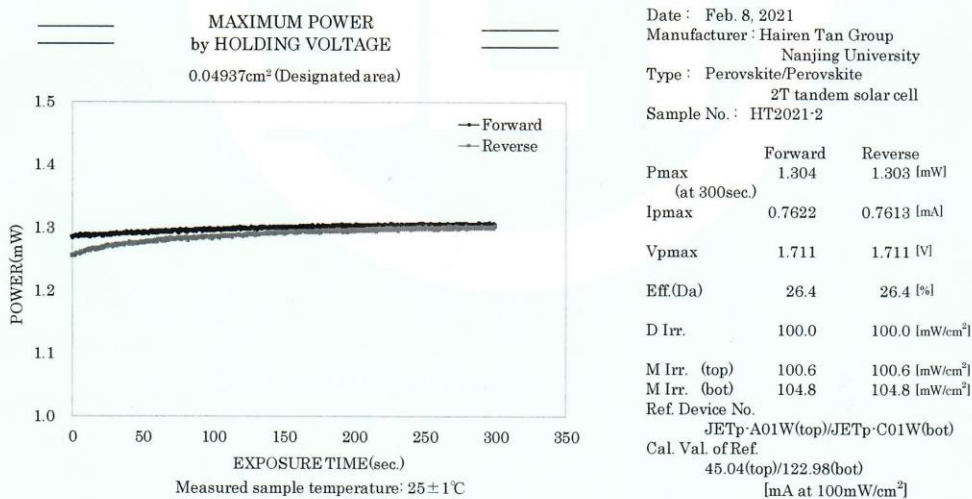
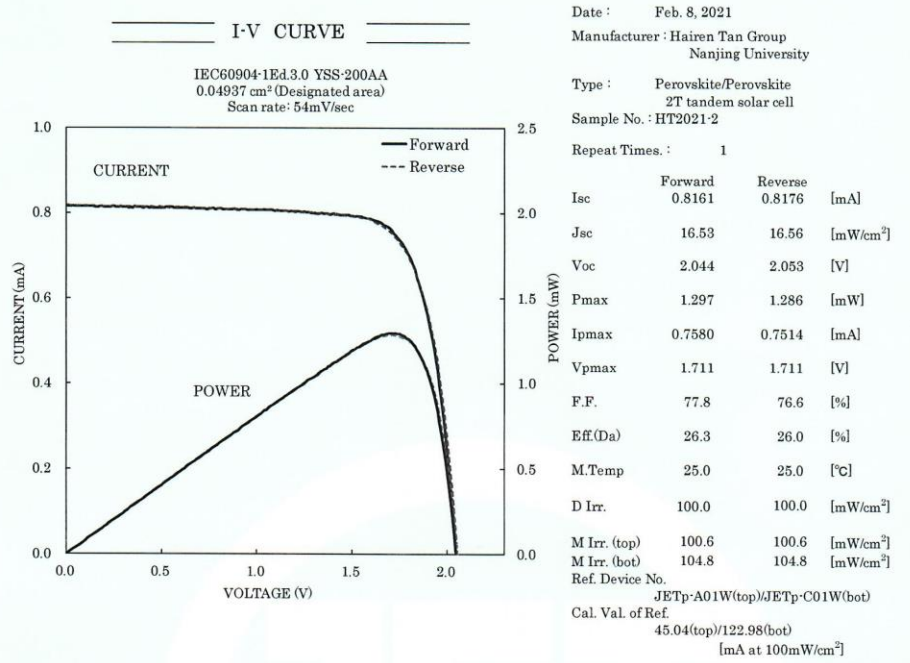


JET



JET

測定成績書番号(Reference No. 20TR-PV0029)

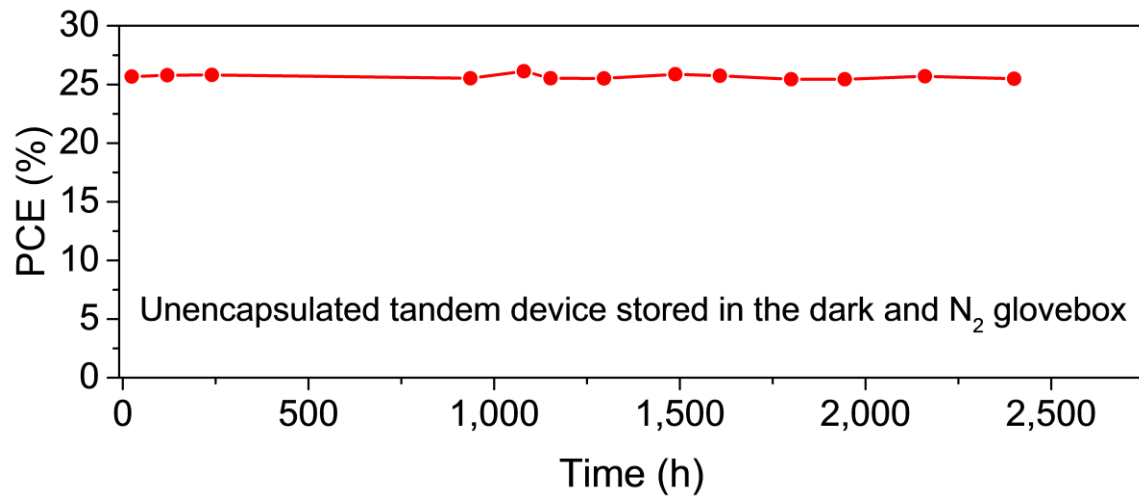


Supplementary Figure 16 | Certified results of two all-perovskite tandem solar cells with CF3-PA. The devices delivered certified stabilized PCEs of 26.4% and 26.1%.

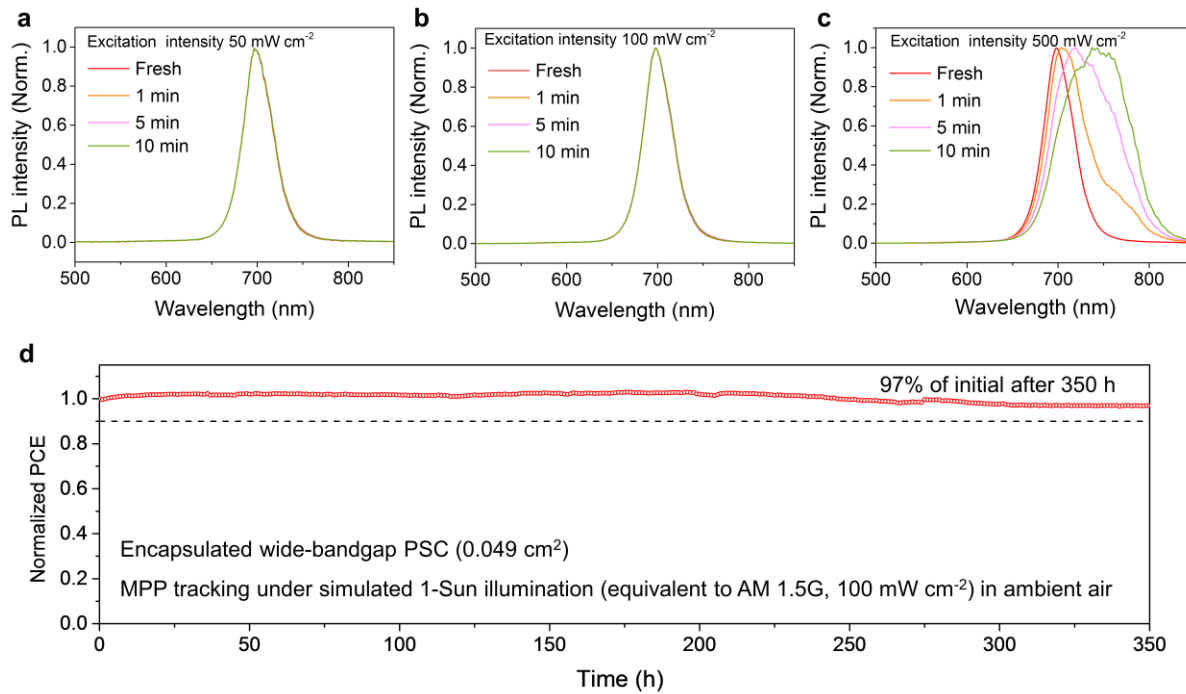
Supplementary Note 4:

A Roadmap to over 30% PCE all-perovskite tandem solar cells

Previous modelling work has suggested that all-perovskite tandems have an empirical efficiency limit of 33.6% (with a J_{sc} of 18.0 mA cm⁻², a V_{oc} of 2.28 V, and an FF of 82%)⁶. To achieve PCEs beyond 30%, one focus will be on improving the V_{oc} of WBG front subcell from 1.22 V reported herein to ~1.4 V, likely achieved by the suppression of bulk and surface recombination⁷. Another focus will be on further improving J_{sc} in tandems by reducing optical losses (reflection and parasitic absorption losses) and by increasing light absorption in Pb-Sn subcells through the use of a thicker absorber layer. Combining these efforts, we anticipate the PCEs of all-perovskite tandem solar cells to approach the performance level of Si/perovskite tandems within the coming years. Developing highly efficient all-perovskite tandem solar cells offer a path to further reduce the leveled cost of electricity in photovoltaics⁸.



Supplementary Figure 17 | Shelf stability of all-perovskite tandem solar cells. The devices were stored under dark in the N₂ glovebox.



Supplementary Figure 18 | Photostability of wide-bandgap perovskites. (a, b and c) PL spectral evolution of perovskite films under different excitation intensity (532 nm laser, intensity equivalent to 50, 100 and 500 mW cm^{-2}) for various duration. (d) MPP tracking of an encapsulated WBG perovskite solar cell under simulated 1-Sun illumination in ambient air.

Supplementary Note 5:

J-V characterization of all-perovskite tandem solar cells

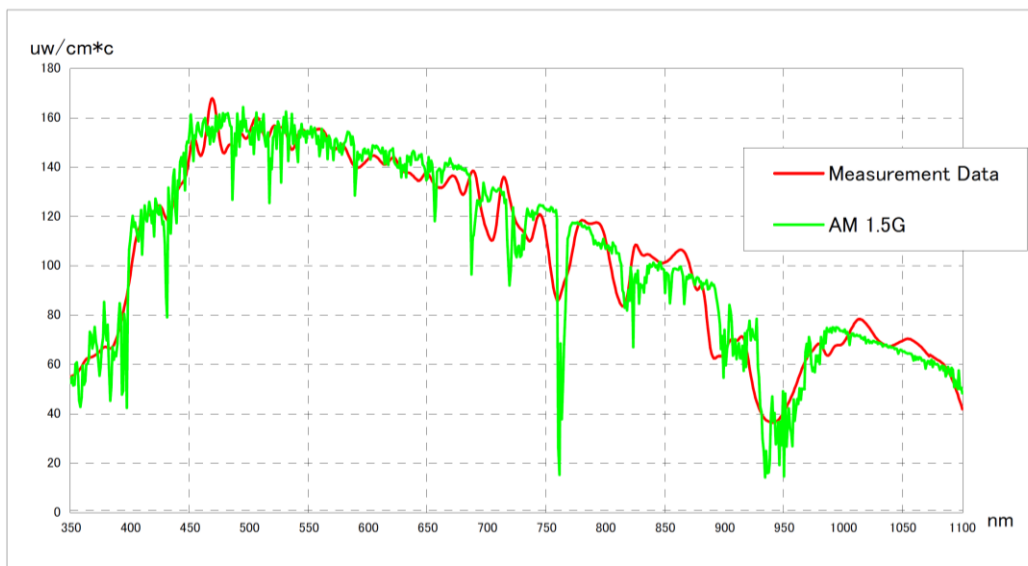
A tandem solar cell consists of two series-connected subcells, and its J-V characteristics is a complex function of the photovoltaic currents generated in each of the junctions. Therefore, the measurement conditions for tandem solar cells should in principle generate photovoltaic currents in each junction similar to those which would be generated in that junction under AM1.5G spectral irradiance. For more details, readers can refer to the IEC Standard (IEC 60904-1-1:2017, Measurement of current-voltage characteristics of multi-junction photovoltaic devices).

The *J-V* characteristics of all-perovskite tandem solar cells presented in this manuscript were measured by a two-lamp simulator, of which the irradiance spectrum is shown in **Supplementary Figure 19**. The spectral mismatch is within $100\pm3\%$ at the wavelength range of 400-1,000 nm, where the all-perovskite tandem solar cells are spectrally sensitive. The spectrum of Xe-lamp based solar simulator is shown in **Supplementary Figure 20**, as compared with AM1.5G. The single Xenon lamp simulator has obvious mismatch with AM1.5G in the near infrared region.

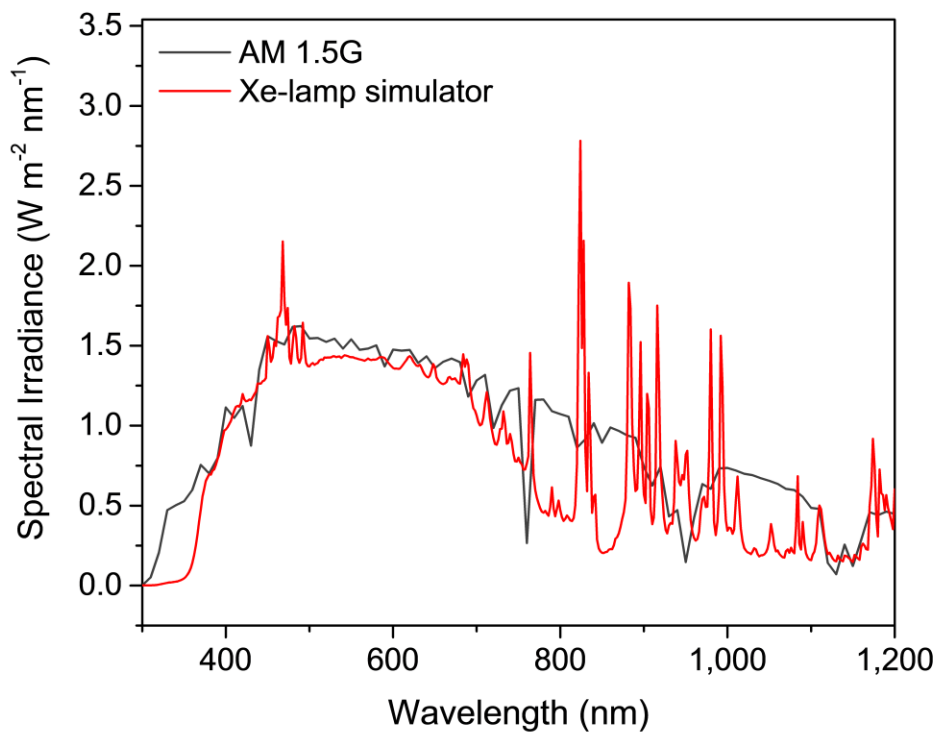
We characterized the *J-V* characteristics of all-perovskite tandem solar cells with three different matching conditions between the front and back subcell: $J_{sc, front} < J_{sc, back}$, $J_{sc, front} = J_{sc, back}$, and $J_{sc, front} > J_{sc, back}$, under two simulators (**Supplementary Figure 21** and **Supplementary Table 5**). Both simulators were calibrated at 1-Sun illumination intensity using KG-5 reference cell. It can be seen that the *FF* values of all the three devices tested under the Xenon lamp is higher than those measurements under the two-lamp simulator. The J_{sc} could be overestimated if the back subcell is the current-limited one. Overall, the measured PCEs under Xe-lamp are higher than those measured under two-lamp simulator, especially for tandem cells that have current-limited back subcells.

Spectral Mismatch (JIS C 8942)

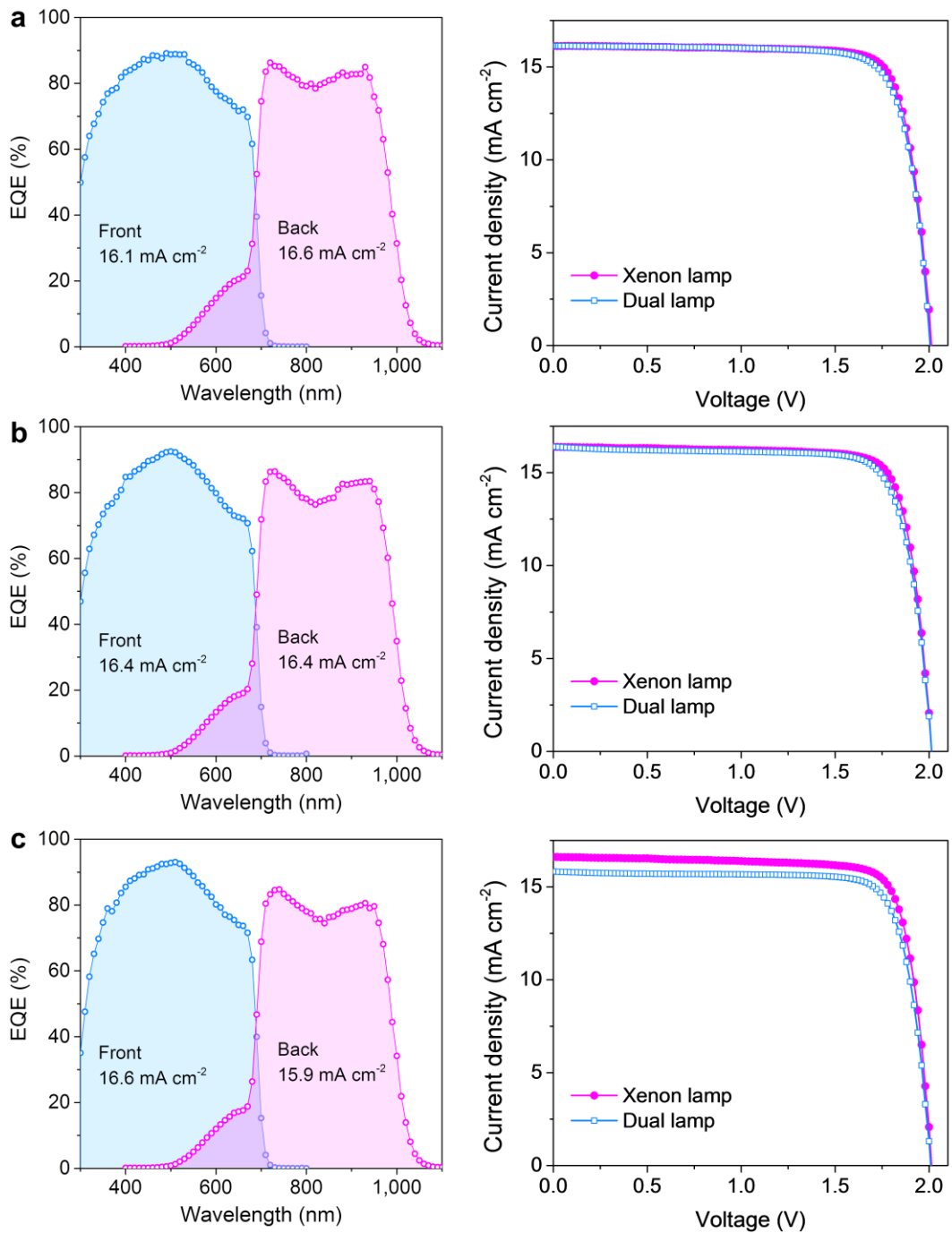
Wave Length	Standard Solar Radiation (%)	Measure Data (%)	Mismatch	JIS Class
350-400	4.09	4.27	104.5%	MS
400-450	7.81	7.77	99.5%	MS
450-500	9.84	9.65	98.1%	MS
500-550	9.66	9.79	101.3%	MS
550-600	9.44	9.38	99.4%	MS
600-650	9.11	8.88	97.5%	MS
650-700	8.50	8.37	98.5%	MS
700-750	7.59	7.53	99.2%	MS
750-800	6.72	6.77	100.8%	MS
800-850	6.16	6.28	102.0%	MS
850-900	5.79	5.63	97.3%	MS
900-950	3.37	3.34	99.1%	MS
950-1000	3.75	3.84	102.5%	MS
1000-1050	4.39	4.56	104.0%	MS
1050-1100	3.78	3.92	103.6%	MS



Supplementary Figure 19| Spectral mismatch of the two-lamp solar simulator used for J-V characterization of all-perovskite tandem solar cells. The spectral mismatch measurement was carried out by San-EI Electric. The red curve (Measurement Data) represents the irradiance spectra of solar simulator.



Supplementary Figure 20 | Spectral irradiance of AM1.5G and Xe-lamp solar simulator.



Supplementary Figure 21 | EQE curves and J - V characteristics of tandem devices with different matching conditions under Xe-lamp and dual-lamp simulators. **a,** $J_{sc, front} < J_{sc, back}$; **b,** $J_{sc, front} = J_{sc, back}$; **c,** $J_{sc, front} > J_{sc, back}$.

Supplementary Tables

Supplementary Table 1. Photovoltaic performance of control, PEA, PA and CF3-PA mixed Pb-Sn perovskite solar cells with an absorber thickness of ~1,200 nm (shown in Fig. 2a). Average performance of 13 devices for each type is presented as well.

Device	V_{oc} (V)	J_{sc} (mA cm ⁻²)	FF (%)	PCE (%)
Control	0.800	31.0	74.1	18.4
Average	0.777±0.014	30.7±0.4	75.0±0.8	17.9±0.3
PEA	0.810	32.0	77.3	20.0
Average	0.797±0.010	31.5±0.2	77.3±0.6	19.4±0.35
PA	0.812	32.5	78.5	20.5
Average	0.804±0.009	31.9±0.5	78.3±0.6	19.9±0.4
CF3-PA	0.838	32.9	79.6	21.9
Average	0.826±0.011	32.5±0.3	78.5±0.7	21.1±0.5

Supplementary Table 2. Photovoltaic performance of representative CF3-PA mixed Pb-Sn perovskite solar cells with absorber thicknesses of 750, 900 and 1,200 nm (shown in Fig. 2b). The devices were processed over the same runs.

Thickness (nm)	V_{oc} (V)	J_{sc} (mA cm ⁻²)	FF (%)	PCE (%)
750	0.825	30.9	78.5	20.0
900	0.825	31.6	78.5	20.6
1200	0.837	32.7	78.9	21.6

Supplementary Table 3. Photovoltaic performance of representative all-perovskite tandem solar cells with NBG absorber thicknesses of 750, 900 and 1,200 nm (shown in Fig. 4b). The devices were processed over the same runs.

NBG thickness	V_{oc} (V)	J_{sc} (mA cm ⁻²)	FF (%)	PCE (%)
750 nm	2.002	15.4	81.0	25.0
900 nm	2.033	16.0	78.5	25.6
1200 nm	2.021	16.5	79.1	26.4

Supplementary Table 4. Independently certified best efficiencies of thin-film solar cells. Data was extracted from the recent *Solar cell efficiency tables* (version 58).

	Cell type	V_{oc} (V)	J_{sc} (mA cm $^{-2}$)	FF (%)	PCE (%)	Group
Single junction	CIGS	0.734	39.58	80.4	23.4	Solar Frontier
	CdTe	0.887	31.69	78.5	22.1	First Solar
	PVK	1.188	25.74	83.2	25.5	UNIST
	OPV	0.896	25.72	78.9	18.2	SHJU/Beihang U
	DSSC	1.020	15.17	79.1	12.2	EPFL
	CZTSSe	0.513	35.21	69.8	12.6	IBM
	nc-Si:H	0.550	29.72	75.0	11.9	AIST
2T-tandem	a-Si/nc-Si	1.342	13.45	70.2	12.7	AIST
	PVK/CIGS	1.768	19.24	72.9	24.2	HZB
	PVK/PVK	2.048	16.54	77.9	26.4	Nanjing U (this work)

Supplementary Table 5. Photovoltaic parameters of tandem solar cells with different matching conditions measured under Xe-lamp and dual-lamp simulators. The *J-V* characteristics of the three tandem devices are shown in **Supplementary Figure 21**.

Sample	Simulator	V_{oc} (V)	J_{sc} (mA/cm²)	FF (%)	PCE (%)
a	Xe lamp	2.013	16.1	81.3	26.4
	Dual lamp	2.005	16.1	79.7	25.8
b	Xe lamp	2.014	16.4	81.3	26.8
	Dual lamp	2.013	16.4	79.1	26.1
c	Xe lamp	2.013	16.6	80.9	27.0
	Dual lamp	2.009	15.8	80.6	25.6

References

1. Kim, D. *et al.* Efficient, stable silicon tandem cells enabled by anion-engineered wide-bandgap perovskites. *Science* **368**, 155–160 (2020).
2. Zheng, X. *et al.* Managing grains and interfaces via ligand anchoring enables 22.3% - efficiency inverted perovskite solar cells. *Nat. Energy* **5**, 131–140 (2020).
3. Jiang, Q. *et al.* Surface passivation of perovskite film for efficient solar cells. *Nat. Photonics* **13**, 460–466 (2019).
4. Ruggeri, E. *et al.* Controlling the Growth Kinetics and Optoelectronic Properties of 2D/3D Lead–Tin Perovskite Heterojunctions. *Adv. Mater.* **31**, 1905247 (2019).
5. Chen, Z. *et al.* Stable Sn/Pb-Based Perovskite Solar Cells with a Coherent 2D/3D Interface. *iScience* **9**, 337–346 (2018).
6. Jošt, M., Kegelmann, L., Korte, L. & Albrecht, S. Monolithic Perovskite Tandem Solar Cells: A Review of the Present Status and Advanced Characterization Methods Toward 30% Efficiency. *Adv. Energy Mater.* **10**, 1904102 (2020).
7. Mahesh, S. *et al.* Revealing the origin of voltage loss in mixed-halide perovskite solar cells. *Energy Environ. Sci.* **13**, 258–267 (2020).
8. Li, Z. *et al.* Cost Analysis of Perovskite Tandem Photovoltaics. *Joule* **2**, 1559–1572 (2018).